Doppler Signature Separation of Mixed O/X-Mode Over-The-Horizon Radar Signals

Ammar Ahmed and Yimin D. Zhang
Department of Electrical and Computer Engineering
College of Engineering, Temple University
Philadelphia, PA 19122, USA

Braham Himed
RF Technology Branch
Air Force Research Laboratory
WPAFB, OH 45433, USA

***Abstract*—In this paper, we consider the Doppler signatures of local multipath target signals in an over-the-horizon radar and the objective is to separate signals corresponding to the ordinary (O) and extraordinary (X) propagation modes. As signals of these two modes are reflected at different ionosphere heights, the rendered Doppler signatures are more complicated and cannot be directly analyzed for parameter estimation using conventional local multipath models which are developed for a single propagation mode. We consider a mixed O/X-mode signal model and analyze the resulting Doppler signatures comprising of more signal components. It is shown that sparsity-based methods estimate the Doppler components with improved resolution and accuracy. Moreover, the proposed group sparsity-based strategy enables separation of the resolved Doppler components corresponding to the two propagation modes. We present the simulation results for a challenging scenario where the multipath Doppler signatures corresponding to the two modes are interlaced.**

keywords: Doppler parameter estimation, fractional Fourier transform, group sparsity, over-the-horizon radar, ordinary and extraordinary modes.

I. Introduction

Sky-wave over-the-horizon radar (OTHR) systems enable surveillance of targets that are beyond the limit of the earth horizon [1–6]. So far, significant research efforts have been dedicated to target parameter estimation in OTHR [7–12]. In this context, an important parameter which facilitates the target classification is the target altitude. In practice, target altitude estimation is very challenging because of the narrowband nature of OTHR sensing signals. Moreover, time-varying ionosphere conditions add further uncertainties and make target altitude estimation more difficult. Existing target altitude estimation techniques in OTHR are generally based on one of the following three major approaches: (a) performing target tracking that includes target altitude information in the target state [8–11, 13–15]; (b) joint estimation of target and ionosphere parameters based on their statistical model [12, 16]; and (c) high-resolution time-frequency analysis of local multipath signal components [17–25]. The proposed work considered in this paper is based on the last approach.

An important strategy to estimate the target altitude for OTHR is to employ the local multipath model [8]. In this model, the OTHR signals back-scattered by the target and received at the radar receivers follow three distinct round-trip paths due to their reflections from the ionosphere and the earth surface. The overall Doppler frequency profile of these three multipath signal components consists of three spectrally equidistant Doppler components. The spectral distance of these three Doppler components and their spectral average enables the estimation of target parameters such as the target elevation velocity and height [17, 20, 21].

In practice, two distinct electromagnetic propagation modes, known as the ordinary (O) and extraordinary (X) modes, may arise in the ionosphere [26–28]. The signals propagating through these two modes are reflected at different ionosphere heights, resulting in different slant ranges and different Doppler signatures for the two modes. Recently, the Doppler signatures of mixed O/X-mode signals was considered in [29], focusing on the detectability of the Doppler parameters when the difference between the reflection heights of both modes is very small.

In this paper, we consider the separation of the Doppler signatures corresponding to the mixed O/X modes when the Doppler difference due to the two modes is comparable to that due to the local multipath. For a target that moves with a constant horizontal velocity and a constant height, we reveal that all Doppler components in both modes exhibit the same chirp rate. As the conventional methods fail to resolve these Doppler components, we exploit Lasso-based approach [30] to achieve high-resolution Doppler frequency estimation of the mixed O/X mode signals which are generally present as six distinct chirp components. Finally, a group sparsity-based strategy [31, 32] is devised to separate the signal components corresponding to the two propagation modes.

Notations: We use lower-case (upper-case) bold characters to denote vectors (matrices). In particular, $(.)^{\mathrm{T}}$ and $(\cdot)^*$ respectively denote the transpose and conjugate operators of a matrix or vector. Moreover, $|\cdot|_1$ and $|\cdot|_2$ respectively denote the l_1- and l_2-norms of a vector. Furthermore, $\mathbf{1}_N$ is the N-length column vector of all ones, $\circ$ is the Hadamard product, and $\sqrt{\cdot}$ denotes the element-wise square root of a vector.

II. Multipath O/X-mode Signal Model

The OTHR signals following the O and X propagation modes are reflected at different ionosphere heights, referred to as the virtual ionosphere heights. These virtual heights usually vary depending on the operating frequency of the OTHR and the incidence angle of the transmitted signals [26–28]. Fig. 1 illustrates the flat-earth multipath signal model by incorporating both O- and X modes of signals. Without loss of generality, we consider that the virtual ionosphere height of the X-mode wave is lower than that of the O-mode wave. In Fig. 1, H denotes the virtual ionosphere height of the O-mode wave whereas $H - \Delta H$ represents that of the

The work of A. Ahmed and Y. D. Zhang is supported in part by a contract with Matrix Research, Inc. for research sponsored by the Air Force Research Laboratory under Contract FA8650-14-D-1722. The work of Y. D. Zhang is also supported in part by a contract with Altamira Technologies Corp. for research sponsored by the Air Force Research Laboratory under Contract FA8650-18-C-1055.

978-1-7281-8942-0/20/$31.00 ©2020 IEEE

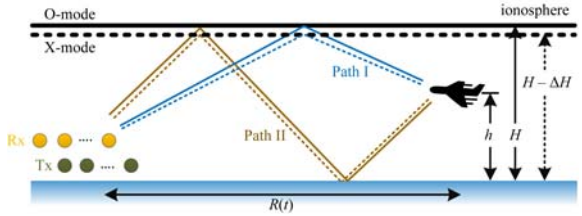

Fig. 1: Flat-earth local multipath propagation model of OTHR for O-mode (solid lines) and X-mode (dashed lines) waves.

X-mode wave with $\Delta H \ll H$. Moreover, h denotes the target altitude. We further assume that a *coarse* estimate of the ionosphere virtual heights is known from, e.g., ionosonde monitoring. We consider stationary ionospheric conditions, i.e., the ionosphere height does not change during the coherent processing interval (CPI) of the OTHR operation, and the target is flying with a fixed altitude and a constant horizontal velocity. For mathematical convenience, we consider that the O- and X-mode signals have the same operating frequency.

It is observed in Fig. 1 that the two propagation modes result in different round-trip paths, which are respectively illustrated as solid and dashed lines. The signals following each propagation mode can either follow path I (reflected only by the ionosphere) or path II (reflected by the ionosphere and the earth surface) for transmission as well as reception. They render three distinct round-trip propagation paths for each propagation mode, given by: (a) transmitted and received along path I; (b) transmitted and received along path II; and (c) transmitted along path I and received along path II, and vice versa.

In the following, we first consider the slant range and the resulting Doppler signatures for the O-mode wave. The results for the X-mode wave can be derived in a similar manner. For the convenience of computing the slant ranges, we convert the multipath signal model for the O-mode wave in Fig. 1 to an equivalent model depicted in Fig. 2 [17, 21], where the target and the propagation paths below the ionosphere layer physically exist, whereas those above the ionosphere layer are their mirrored images due to the reflections at the ionosphere and the earth surface.

The one-way slant ranges of paths I and II for the O-mode wave, respectively denoted as $l_{\mathrm{o},1}$ and $l_{\mathrm{o},2}$, can be expressed in terms of the ground range R, the virtual ionosphere height H, and the target altitude h, as follows:

$$l_{\mathrm{o},1} = \left(R^2 + (2H-h)^2\right)^{1/2}, \quad l_{\mathrm{o},2} = \left(R^2 + (2H+h)^2\right)^{1/2}. \tag{1}$$

Due to the non-zero horizontal target velocity, its ground range R varies with time. This means that the slant ranges $l_{\mathrm{o},1}$ and $l_{\mathrm{o},2}$ are both time-varying. Note that the explicit notation of (t) is omitted for rotational brevity.

In practical OTHR operations, $h \ll H \ll R$ holds. In this case, we can expand Eq. (1) by employing the Taylor approximation as:

$$l_{\mathrm{o},1} \approx R + \frac{2H^2 - 2Hh}{R}, \quad l_{\mathrm{o},2} \approx R + \frac{2H^2 + 2Hh}{R}. \tag{2}$$

As a result, the slant range of the three round-trip paths can be respectively expressed as:

$$L_{\mathrm{o},1} = 2l_{\mathrm{o},1}, \quad L_{\mathrm{o},2} = 2l_{\mathrm{o},2}, \quad L_{\mathrm{o},3} = l_{\mathrm{o},1} + l_{\mathrm{o},2}. \tag{3}$$

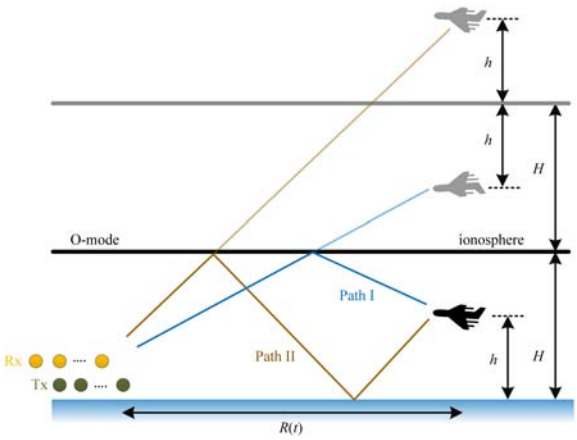

Fig. 2: Equivalent local multipath propagation model for the O-mode wave.

For the case of X-mode signals, we can derive similar slant range equations by substituting H with $H - \Delta H$ in Eq. (2).

III. Doppler Signature Analysis

The Doppler signatures due to the O-mode signal propagation through the three round-trip paths in Eq. (3) can be expressed as $f_{\mathrm{o},i} = -(f_c/c)\mathrm{d}L_{\mathrm{o},i}/\mathrm{d}t$ for $i = 1, 2, 3$, where c is the velocity of the electromagnetic wave, f_c is the carrier frequency, and i denotes the path index. By exploiting Eq. (2), we obtain:

$$\frac{\mathrm{d}l_{\mathrm{o},1}}{\mathrm{d}t} \approx \dot{R} - 2\frac{H\dot{R}}{R^2}(H-h), \quad \frac{\mathrm{d}l_{\mathrm{o},2}}{\mathrm{d}t} \approx \dot{R} - 2\frac{H\dot{R}}{R^2}(H+h), \tag{4}$$

where $\dot{R} = \mathrm{d}R/\mathrm{d}t$ denotes the target horizontal velocity. The target velocity is considered positive when the target is moving away from the radar. Denote the average Doppler frequency and intra-mode Doppler difference for O-mode signals as $\bar{f}_{\mathrm{o}}$ and Δf_{o}, respectively, given by:

$$\begin{aligned} \bar{f}_{\mathrm{o}} &= -\frac{f_c}{c}\frac{\mathrm{d}(l_{\mathrm{o},1} + l_{\mathrm{o},2})}{\mathrm{d}t} \approx -\frac{2f_c}{c}\dot{R} + \frac{4f_c H^2 \dot{R}}{cR^2}, \\ \Delta f_{\mathrm{o}} &= -\frac{f_c}{c}\frac{\mathrm{d}(l_{mo,1} - l_{\mathrm{o},2})}{\mathrm{d}t} \approx -\frac{4f_c Hh\dot{R}}{cR^2}. \end{aligned} \tag{5}$$

Then, the Doppler frequencies corresponding to the three different round-trip paths of the O-mode wave take the following simplified form:

$$f_{\mathrm{o},1} = \bar{f}_{\mathrm{o}} + \Delta f_{\mathrm{o}}, \quad f_{\mathrm{o},2} = \bar{f}_{\mathrm{o}} - \Delta f_{\mathrm{o}}, \quad f_{\mathrm{o},3} = \bar{f}_{\mathrm{o}}, \tag{6}$$

From Eqs. (5)–(6), we notice that the Doppler signatures of the round-trip paths 1 and 2 are symmetric around the round-trip path 3. The average Doppler component for the O-mode wave, $\bar{f}_{\mathrm{o}}$, is shared by all three round-trip paths, whereas the intra-mode Doppler difference for the O-mode wave Δf_{o} denotes the frequency difference between any two adjacent O-mode Doppler components. It is clear that both $\bar{f}_{\mathrm{o}}$ and Δf_{o} are proportional to $\dot{R}$.

Similarly, we can formulate the Doppler components associated with the X-mode wave as:

$$f_{\mathrm{x},1} = \bar{f}_{\mathrm{x}} + \Delta f_{\mathrm{x}}, \quad f_{\mathrm{x},2} = \bar{f}_{\mathrm{x}} - \Delta f_{\mathrm{x}}, \quad f_{\mathrm{x},3} = \bar{f}_{\mathrm{x}}, \tag{7}$$

where the average Doppler component of the X-mode signals $\bar{f}_{\rm x}$ and the corresponding intra-mode Doppler difference $\Delta f_{\rm x}$ are obtained by replacing H with $H-\Delta H$ in Eq. (5) as:

$$\begin{aligned}\bar{f}_{\rm x} &\approx -\frac{2f_c}{c}\dot{R}+\frac{4f_c(H-\Delta H)^2\dot{R}}{cR^2}\\ &= \bar{f}_{\rm o}-\frac{4f_c\dot{R}}{cR^2}(2H\Delta H-\Delta H^2),\\ \Delta f_{\rm x} &\approx -\frac{4f_c(H-\Delta H)h\dot{R}}{cR^2}=\Delta f_{\rm o}+4\frac{f_c h\dot{R}}{cR^2}\Delta H.\end{aligned} \tag{8}$$

Considering a typical scenario with $h \ll R$ and $\Delta H \ll R$, we observe the following relationship:

$$\bar{f}_{\rm x} \approx \bar{f}_{\rm o}-f_\delta, \quad \Delta f_{\rm x} \approx \Delta f_{\rm o}, \tag{9}$$

where $f_\delta \approx (4f_c\dot{R}/(cR^2))(2H\Delta H-\Delta H^2)$ is an unknown inter-mode Doppler difference depicting the spectral distance between the average Doppler components of the signals associated with the two propagation modes.

From Eqs. (5)–(9), we observe that the inter-mode Doppler difference f_δ is shared for all the local multipath pairs of corresponding O/X-mode signals, i.e.,

$$f_\delta = f_{{\rm o},i}-f_{{\rm x},i}, \quad i=1,2,3. \tag{10}$$

This shows that the three Doppler components respectively generated by O- and X-mode waves are displaced in the spectral domain by a common shift f_δ.

IV. Group Sparsity-based Doppler Separation

A. Signal Formulation

At the OTHR receiver, we express the overall noise-free signal following the O/X-mode propagation as follows:

$$y(t)=\sum_{i=1}^{3}\Big(A_{{\rm o},i}e^{j(2\pi\int_0^T f_{{\rm o},i}{\rm d}t+\phi_{{\rm o},i})}+A_{{\rm x},i}e^{j(2\pi\int_0^T f_{{\rm x},i}{\rm d}t+\phi_{{\rm x},i})}\Big), \tag{11}$$

where $A_{{\rm o},i}$ and $A_{{\rm x},i}$ respectively denote the signal magnitudes for the signals following the O and X modes, $\phi_{{\rm o},i}$ and $\phi_{{\rm x},i}$ are the corresponding initial phases, and T is the CPI duration. Note that $f_{{\rm o},i}$ and $f_{{\rm x},i}$ are time-varying. Substituting Eq. (10) in Eq. (11), we reformulate $y(t)$ as:

$$\begin{aligned}y(t) = \sum_{i=1}^{3}\Big(&A_{{\rm o},i}e^{j(2\pi\int_0^T f_{{\rm o},i}{\rm d}t+\phi_{{\rm o},i})}\\ &+A_{{\rm x},i}e^{j(2\pi\int_0^T (f_{{\rm o},i}+f_\delta){\rm d}t+\phi_{{\rm x},i})}\Big).\end{aligned} \tag{12}$$

If the inter-mode Doppler difference f_δ is very small, the O- and X-mode Doppler components merge together in the spectral domain. The Doppler frequency resolution for this case was discussed in [29]. On the other hand, if f_δ is large ($f_\delta \gg 3\Delta f_{\rm o}$), the resulting Doppler signatures of the two modes are distantly separated in the spectral domain, thus facilitating the Doppler signature separation. The Doppler signature separation is more challenging if the Doppler frequency profiles of the two propagation modes are either very close to each other or interlaced in the spectral domain. Such situations usually arise when $f_\delta \le 3\Delta f_{\rm o}$.

Let us examine the Doppler frequency components generated from the O- and X-mode waves for the parameters listed in Table I, given that $\Delta H = 15$ km. The corresponding spectrally interlaced Doppler profile for both propagation modes is illustrated in Fig. 3(a) whereas the spectrogram and the fractional Fourier transform (FrFT) magnitude are respectively shown in Figs. 3(b) and 3(c). It is observed that the six Doppler components are interlaced and difficult to separate. From Fig. 3(d), we find the peak value for the rotation angle and the six frequency peaks corresponding to the six Doppler components. However, the frequency resolution is rather poor. The example in Fig. 3 clearly shows the challenges in identifying the average Doppler and the difference Doppler using the existing techniques when the Doppler signatures corresponding to the mixed O/X-mode signals interlace.

TABLE I: Simulation Parameters

Parameter	Notation	Value
Initial range	$R(0)$	2,500 km
O-mode ionosphere height	H	350 km
X-mode ionosphere height	$H-\Delta H$	335 km
Target altitude	h	20 km
Target horizontal velocity	$\dot{R}$	400 m/s
Carrier frequency	f_c	16 MHz
Pulse repetition frequency	f_s	100 Hz
Coherent integration time	T	80 s
Signal-to-noise ratio (SNR)	η	0 dB

B. Sparsity-based Doppler Signature Separation

We devise sparsity-based Doppler signature separation by exploiting the de-chirped version of the received signal $y(t)$ to achieve improved resolution. As discussed in Section III and observed in Fig. 3, all six Doppler components share the same chirp rate which can be estimated by exploiting the peak rotation angle $\alpha_{\rm opt}$ from the FrFT as [33, 34]:

$$\hat{\gamma} = -\cot\left(\alpha_{\rm opt}\frac{\pi}{2}\right)\frac{f_s^2}{N}, \tag{13}$$

where f_s is the pulse repetition frequency and N is the number of samples used in the FrFT computation. Subsequently, the received signal $y(t)$ in Eq. (11) is de-chirped as:

$$\begin{aligned}\bar{y}(t) &= y(t)e^{-j2\pi\hat{\gamma}t^2/2},\\ &\approx \sum_{i=1}^{3}\left(A_{{\rm o},i}e^{j(2\pi f^{\rm s}_{{\rm o},i}t+\phi_{{\rm o},i})}+A_{{\rm x},i}e^{j\left(2\pi f^{\rm s}_{{\rm x},i}t+\phi_{{\rm x},i}\right)}\right),\end{aligned} \tag{14}$$

where $f^{\rm s}_{{\rm o},i}$ and $f^{\rm s}_{{\rm x},i}$ represent the start frequencies, respectively for the two modes after de-chirpping. In order to determine these start frequencies, we first construct an N-length data vector $\bar{\mathbf{y}}$ from the sampled de-chirped signal $\bar{y}(t)$ as $\bar{\mathbf{y}} = [\bar{y}(t), \bar{y}(t-1), \cdots, \bar{y}(t-N)]^{\rm T}$. Subsequently, sparse frequency estimation over the grid $\mathcal{F}$ of R frequencies are achieved using the Lasso as [30]:

$$\hat{\mathbf{r}} = \arg\min_{\mathbf{r}} \quad |\bar{\mathbf{y}}-\mathbf{F}\mathbf{r}|_2^2+\zeta|\mathbf{r}|_1, \tag{15}$$

where $\mathbf{F}$ is the $N\times R$ Fourier transform dictionary matrix with each of its columns corresponding to a frequency in $\mathcal{F}$, $\mathbf{r}$ is the sparse column vector of length R, and $\zeta > 0$ is a regularization parameter. The positions of the non-zero elements of the obtained solution $\hat{\mathbf{r}}$ correspond to the estimated Doppler

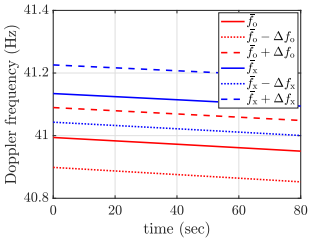

(a) Actual Doppler signatures

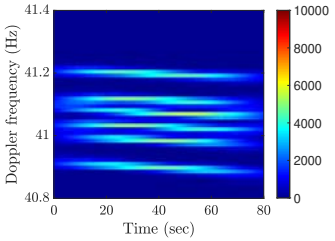

(b) Spectrogram

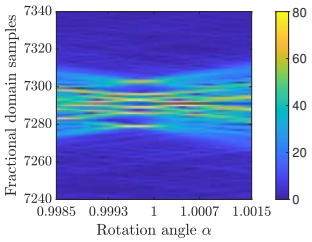

(c) Fractional Fourier transform (FrFT)

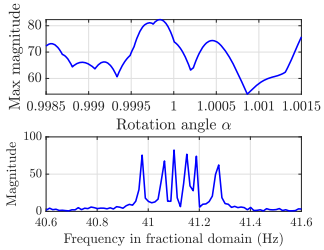

(d) Chirp rate and spectrum estimation using FrFT

Fig. 3: Doppler frequency estimation using conventional time-frequency methods (for $\Delta H = 15$ km).

frequencies in the search grid which are present in the de-chirped signal vector $\bar{\mathbf{y}}$. Fig. 4(a) shows the estimated Doppler signatures using Lasso for the six Doppler components shown in Fig. 3(a). It is clear that, unlike the spectrogram shown in Fig. 3(b) and FrFT shown in Figs. 3(c) and 3(d), the Lasso optimization (15) provides high-resolution estimates of all six Doppler components. However, it remains unclear in Fig. 4(a) whether a specific Doppler component belongs to the O or the X mode. This issue is discussed in the subsequent subsection.

C. Group Sparsity-based Doppler Signature Separation

It is observed in Fig. 3(d) and 4(a) that, when the frequency profiles of the mixed O/X-mode signals interlace, automatic separation of the two modes of spectral components becomes difficult. In order to address this problem, we propose a group sparsity-based approach to utilize the spectral structure of the Doppler signatures. Using Eqs. (9) and (14), we obtain:

$$\bar{y}(t) \approx \sum_{i=1}^{3} \left(A_{\mathrm{o},i} e^{j(2\pi f^{\mathrm{s}}_{\mathrm{o},i} t + \phi_{\mathrm{o},i})} + A_{\mathrm{x},i} e^{j\left(2\pi \left(f^{\mathrm{s}}_{\mathrm{o},i} + f_\delta\right) t + \phi_{\mathrm{x},i}\right)} \right). \tag{16}$$

Eq. (16) shows that the Doppler components corresponding to the two modes form two separate groups, each containing three components. The two groups of the Doppler components are separated by f_δ but otherwise have nearly identical structures.

Denote $\mathbf{r}_1$ and $\mathbf{r}_2$ as two unknown sparse vectors that are defined on their respective search grids $\mathcal{F}$ and $\mathcal{F} + f_\delta$, and let $\mathbf{F}_1$ and $\mathbf{F}_2$ be their respective Fourier transform dictionary matrices. Note that the spectral distance between the corresponding columns of $\mathbf{F}_1$ and $\mathbf{F}_2$ is equal to f_δ. The resulting group of the sparse vectors can be written in a matrix form as $\mathbf{R} = [\mathbf{r}_1, \mathbf{r}_2]$. We devise the sparse-group Lasso formulation as [31]:

$$\begin{aligned} \hat{\mathbf{r}}_1 = \arg \min_{\mathbf{r}_1, \mathbf{r}_2} [& |\bar{\mathbf{y}} - \mathbf{F}_1 \mathbf{r}_1 - \mathbf{F}_2 \mathbf{r}_2|_2^2 \\ & + \zeta \left(\kappa |\mathbf{R}|_{1,2} + (1-\kappa) |\mathbf{R}|_1 \right)], \end{aligned} \tag{17}$$

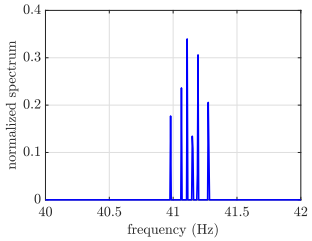

(a) Using Lasso

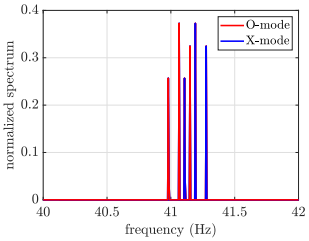

(b) Using sparse-group Lasso

Fig. 4: Sparsity-based Doppler frequency estimation.

where

$$|\mathbf{R}|_{1,2} = \mathbf{1}_N^{\mathrm{T}} \sqrt{(\mathbf{r}_1 \circ \mathbf{r}_1^* + \mathbf{r}_2 \circ \mathbf{r}_2^*)} \tag{18}$$

is the mixed $l_{1,2}$-norm of matrix $\mathbf{R}$ and

$$|\mathbf{R}|_1 = \max_{k=1,2} \left(\sum_{i=1}^{N} |R(i,k)| \right) \tag{19}$$

is the l_1-norm of matrix $\mathbf{R}$ defined as its maximum of absolute column sum, with $R(i,k)$ denoting the (i,k)th element of $\mathbf{R}$. The optimization problem (17) groups the sparse vectors $\mathbf{r}_1$ and $\mathbf{r}_2$ by exploiting the mixed $l_{1,2}$-norm of sparse matrix $\mathbf{R}$ and also encourages intra-group sparsity by employing the matrix l_1-norm. The selection of parameter $\kappa \in [0,1]$ in (17) provides a convex combination of Lasso [30] and group Lasso [32] penalties ($\kappa = 0$ gives Lasso fit, $\kappa = 1$ gives group Lasso fit). Thus, κ trades off between the inter- and the intra-group sparsity in optimization (17) [31]. Intra-group sparsity is specifically important to keep the non-zero components within each group (mode) to be a minimum value of 3.

Note that the parameter f_δ required in (17) is unknown. Given the six component sparse spectrum obtained in Fig. 4(a), there are only three possible values that f_δ can take. We repeat the optimization in (17) for all three possible values of f_δ and the correct value renders three distinct peaks for each of the sparse vectors $\mathbf{r}_1$ and $\mathbf{r}_2$. Fig. 4(b) shows the estimates of the start Doppler frequencies for O- and X-mode signals which correspond to the sparse vectors $\mathbf{r}_1$ and $\mathbf{r}_2$. The well-separated clean results in Fig. 4(b) show three respective peaks for each mode illustrating that the inter- and intra-mode Doppler frequency difference and the average Doppler frequencies are adequately separated, thereby enabling target parameter estimation.

V. Conclusion

In this paper, we have investigated mixed O/X-mode OTHR signals when the virtual ionospheric heights for both modes exhibit a small height difference. When the Doppler frequency components of the two modes are interlaced or closely separated, it is challenging to separate their respective Doppler frequency profiles. We proposed a sparsity-based frequency estimation approach to resolve the six Doppler components with high resolution. Moreover, we further developed a group sparsity-based methods to separate the respective Doppler signatures of the O- and X-mode signals, thereby enabling the estimation of target motion parameters.

VI. REFERENCES

[1] M. Headrick and M. I. Skolnik, "Over-the-horizon radar in the HF band," *Proc. IEEE*, vol. 62, no. 6, pp. 664–673, June 1974.

[2] A. A. Kolosov, *Over-the-Horizon Radar*. Artech House, 1987.

[3] G. J. Frazer, Y. Abramovich, B. A. Johnson, "Use of adaptive non-causal transmit beamforming in OTHR: Experimental results," in *Proc. Int. Conf. Radar*, Adelaide, Australia, Sept. 2008, pp. 311–316.

[4] J. M. Headrick and S. J. Anderson, "HF over-the-horizon radar," Chapter 20 in M. Skolnik (ed.), *Radar Handbook, 3rd Ed.* McGraw-Hill, 2008.

[5] G. A. Fabrizio, *High Frequency Over-the-Horizon Radar: Fundamental Principles, Signal Processing, and Practical Applications*. McGraw-Hill, 2013.

[6] G. J. Frazer, "Experimental results for MIMO methods applied in over-the-horizon radar," *IEEE Aerosp. Electron. Syst. Mag.*, vol. 32, no. 12, pp. 52–69, Dec. 2017.

[7] W. Wang, Y. Peng, T. Quan, and Y. Liu, "HF OTHR target detection and estimation subsystem," *IEEE Aerosp. Electron. Syst. Mag.*, vol. 14, no. 4, pp. 39–45, April 1999.

[8] R. H. Anderson, S. Kraut, and J. L. Krolik, "Robust altitude estimation for over-the-horizon radar using a state-space multipath fading model," *IEEE Trans. Aerospace Electron. Syst.*, vol. 39, no. 1, pp. 192–201, Mar. 2003.

[9] D. Bourgeois, C. Morisseau, and M. Flecheux, "Over-the-horizon radar target tracking using multi-quasi-parabolic ionospheric modelling," *IEE Proceedings - Radar, Sonar and Navig.*, vol. 153, no. 5, pp. 409-416, Oct. 2006.

[10] K. Bell, "MAP-PF multi-mode tracking for over-the-horizon radar," in *Proc. IEEE Radar Conf.*, Atlanta, GA, May 2012, pp. 326–331.

[11] H. Lan, Y. Liang, Q. Pan, F. Yang, and C. Guan, "An EM algorithm for multipath state estimation in OTHR target tracking," *IEEE Trans. Signal Process.*, vol. 62, no. 11, pp. 2814-2826, June 2014.

[12] J. Hu, M. Li, Q. He, Z. He, and R. S. Blum, "Joint estimation of MIMO-OTH radar measurements and ionospheric parameters," *IEEE Trans. Aerospace Electron. Syst.*, vol. 53, no. 6, pp. 2789–2805, June 2017.

[13] S. J. Anderson, "Target altitude estimation in OTHR via diffuse surface scatter," in *Proc. IET Int. Radar Conf.*, Hangzhou, China, April 2015, pp. 1–6.

[14] H. Geng, Y. Liang, F. Yang, L. Xu, and Q. Pan, "Joint estimation of target state and ionospheric height bias in over-the-horizon radar target tracking," *IET Radar, Sonar & Navig.*, vol. 10, no. 7, pp. 1153–1167, Aug. 2016.

[15] H. Lan, Y. Liang, Z. Wang, F. Yang, and Q. Pan, "Distributed ECM algorithm for OTHR multipath target tracking with unknown ionospheric heights," *IEEE J. Sel. Topics Signal Process.*, vol. 12, no. 1, pp. 61–75, Feb. 2018.

[16] Z. Luo, Z. He, X. Chen, and K. Lu, "Target location and height estimation via multipath signal and 2D array for sky-wave over-the-horizon radar," *IEEE Trans. Aerospace Electron. Syst.*, vol. 52, no. 2, pp. 617–631, April 2016.

[17] Y. D. Zhang, M. G. Amin, and G. J. Frazer, "High-resolution time-frequency distributions for manoeuvring target detection in over-the-horizon radars," *IEE Proc.-Radar Sonar Navig.*, vol. 150, no. 4, pp. 299–304, Aug. 2003.

[18] C. Ioana, M. G. Amin, Y. D. Zhang, and F. Ahmad, "Characterization of Doppler effects in the context of over-the-horizon radar," in *Proc. IEEE Radar Conf.*, Washington, D.C., May 2010, pp. 506–510.

[19] C. Ioana, Y. D. Zhang, M. G. Amin, F. Ahmad, G. Frazer, and B. Himed, "Time-frequency characterization of micro-multipath signals in over-the-horizon radar," in *Proc. IEEE Radar Conf.*, Atlanta, GA, May 2012, pp. 671–675.

[20] Y. D. Zhang, M. G. Amin, and B. Himed, "Altitude estimation of maneuvering targets in MIMO over-the-horizon radar," in *Proc. IEEE Sensor Array and Multichannel Signal Process. Workshop*, Hoboken, NJ, June 2012, pp. 257–260.

[21] Y. D. Zhang, J. J. Zhang, M. G. Amin, and B. Himed, "Instantaneous altitude estimation of maneuvering targets in over-the-horizon radar exploiting multipath Doppler signatures," *EURASIP J. Adv. Signal Process.*, vol. 2013, no. 2013:100, pp. 1–13, May 2013.

[22] C. Hou, Y. Wang, and J. Chen, "Estimating target heights based on the Earth curvature model and micromultipath effect in skywave OTH radar," *J. Applied Math.*, vol. 2014, article ID 424191, pp. 1–14, July 2014.

[23] J. Hu, X. He, W. Li, H. Ai, H. Li, and J. Xie, "Parameter estimation of maneuvering targets in OTHR based on sparse time-frequency representation," *J. Systems Eng. Electron.*, vol. 27, no. 3, pp. 574–580, June 2016.

[24] Y. D. Zhang and B. Himed, "Multipath Doppler difference estimation in over-the-horizon radar," in *Proc. IEEE Radar Conf.*, Oklahoma City, OK, April 2018.

[25] V. S. Amin, Y. D. Zhang, and B. Himed, "Group sparsity-based local multipath Doppler difference estimation in over-the-horizon radar," in *Proc. IEEE Int. Radar Conf.*, Rockville, MD, May 2020.

[26] J. M. Kelso, *Radio Ray Propagation in the Ionosphere*. McGraw-Hill, 1964.

[27] K. G. Budden, *The Propagation of Radio Waves: The Theory and Radio Waves of Low Power in the Ionosphere and Magnetosphere*. Cambridge University Press, 1985.

[28] T. J. Harris, M. A. Cervera, L. H. Pederick, and A. D. Quinn, "Separation of O/X polarization modes on oblique ionospheric soundings," *Radio Sci.*, vol. 52, pp. 1522–1533, Oct. 2017.

[29] A. Ahmed, Y. D. Zhang, and B. Himed, "Doppler signature analysis of mixed O/X-mode signals in over-the-horizon radar," in *Proc. IEEE Int. Radar Conf.*, Rockville, MD, May 2020.

[30] R. Tibshirani, "Regression shrinkage and selection via the lasso," *J. R. Stat. Soc. B*, vol. 58, no. 1, pp. 267–288, 1996.

[31] N. Simon, J. Friedman, T. Hastie, and R. Tibshirani, "A sparse-group lasso," *J. Comput. Graph. Stat.*, vol. 22, no. 2, pp. 231–245, May 2013.

[32] N. Simon and R. Tibshirani, "Standardization and the group lasso penalty," *Stat. Sin.*, vol. 22, no. 3, pp. 983–1001, June 2012.

[33] E. Sejdić, I. Djurović, and L. Stanković, "Fractional Fourier transform as a signal processing tool: An overview of recent developments," *Signal Process.*, vol. 91, no. 6, pp. 1351–1369, June 2011.

[34] H. M. Ozaktas, M. A. Kutay, and Z. Zalevsky, *The Fractional Fourier Transform: With Applications in Optics and Signal Processing*. Wiley, 2001.